

# Squeezing of thermal fluctuations in a driven nanomechanical resonator

J. S. Huber<sup>1</sup>, G. Rastelli<sup>1</sup>, M. J. Seitner<sup>1</sup>, J. Kölbl<sup>1\*</sup>, W. Belzig<sup>1</sup>, M. I. Dykman<sup>2</sup>, & E. M. Weig<sup>1</sup>

<sup>1</sup>*Department of Physics, University of Konstanz, 78457 Konstanz, Germany*

<sup>2</sup>*Michigan State University, East Lansing, MI 48824, USA*

Classical squeezing allows manipulating the noise distribution of thermal fluctuations by suppressing the noise along one of the two quadratures. Squeezing of thermal fluctuations has mostly been studied in parametric amplifiers, including realizations based on microwave<sup>1,2</sup> or mechanical<sup>3,4</sup> resonators as well as trapped ions,<sup>5</sup> and is typically detected in a homodyne measurement. Here we show thermal squeezing of a nanomechanical resonator of ultra-high quality factor at room temperature. Squeezing is accomplished by driving the resonator in the nonlinear Duffing regime. Contrary to previous studies,<sup>4,7,8</sup> auxiliary noise injection into the system is not required. Remarkably, the squeezing manifests itself directly in the power spectrum without the need of a homodyne measurement. Classical noise squeezing promises to reduce heating in computers,<sup>9</sup> and represents an important asset for precision sensing<sup>5,10,11</sup> enabling the advent of a new generation of nanomechanical detectors at room temperature.

Originally, squeezing has been considered as a resource to control quantum fluctuations of

---

\*Present address: Department of Physics, University of Basel, 4056 Basel, Switzerland

a system. The Heisenberg uncertainty principle sets a fundamental limit on the fluctuations of two conjugate observables, such as position and momentum or two quadratures of a harmonic oscillator. In the ground state of a harmonic oscillator the uncertainties of the quadratures are equal and minimal, which determines the fundamental quantum limit of their fluctuations. The equality of the uncertainties is a consequence of the time translation symmetry: indeed, changing the time by half the oscillation period leads to the interchange of the quadratures. Squeezing provides a means for redistributing the fluctuations between the quadratures, reducing the uncertainty in one of them below the quantum limit.<sup>12</sup> Quantum squeezing was first detected in quantum optics,<sup>13</sup> and recently also in mechanical systems.<sup>14–16</sup> It enables precision measurements surpassing the quantum limit.<sup>17,18</sup>

The concept of squeezing of fluctuations in vibrational systems is not limited to the quantum regime. Squeezing of thermal fluctuations has been also intensely studied. It is frequently accomplished using parametric pumping or radiation pressure and has been demonstrated for microwave<sup>1,2</sup> and mechanical<sup>3,4,11,14,19–22</sup> resonators as well as for ions in a Penning trap.<sup>5</sup> The classical two-mode squeezing of mechanical resonators by non-degenerate parametric amplification has been also reported.<sup>23–25</sup>

One of the most simple systems that should display classical squeezing is a resonantly driven Duffing resonator.<sup>1–3</sup> The squeezing here is in many respects qualitatively different from what happens in parametric amplifiers, as there is only one mode involved and the squeezing relies on a different type of the nonlinearity. So far, squeezing of an auxiliary noise injected into the system

has been accomplished for a driven Duffing resonators only close to the cusp bifurcation point.<sup>7</sup> In this interesting work the measurement was performed for a nonthermal noise and the squeezing was detected using a homodyne measurement technique, the standard technique to reveal the squeezing of a quadrature; however, only a bound on the actual squeezing could be inferred.

Here we find that the thermal fluctuations of a resonantly driven nonlinear resonator display squeezing in a broad parameter range. Physically, this is a consequence of the breaking of the time translation symmetry by the periodic drive: fluctuations of a vibration quadrature depend on its phase with respect to the drive and can be larger or smaller than in the absence of the drive. Most importantly, we find that the squeezing is directly manifested in the power spectrum of the resonator. This obviates the need of the conventional homodyne detection. We report the distinct and clear observation of thermal squeezing of a high quality factor nanomechanical resonator at room temperature. Under sufficiently strong driving the nonlinear resonator generates two perfectly resolved peaks at satellite frequencies in the power spectrum, which allow extracting the squeezing parameter directly from their area ratio. Contrary to previous studies,<sup>4,7</sup> auxiliary noise injection is not required to reveal the signatures of the squeezed state. The experimental results agree, with no adjustable parameters, with the theory that extends the former predictions.<sup>1-3,7</sup>

In addition, a driven Duffing resonator provides the means for exploring, quantitatively, generic features of thermal fluctuations in a system far away from thermal equilibrium. One of them is fluctuation-induced switching between coexisting stable states. Such switching has been well understood in equilibrium systems.<sup>30</sup> With our high quality factor mechanical resonator we

directly observe thermally induced switching between the coexisting stable vibrational states. We find the parameter values where the state populations are equal, on average. To the best of our knowledge, this is the first time where, for a system with no detailed balance, such parameter values can be quantitatively compared with a theory.

The classical nanomechanical Duffing resonator is realized by a freely-suspended silicon nitride string fabricated on a fused silica substrate.<sup>12</sup> The string under investigation is 270 nm wide, 100 nm thick and 55  $\mu\text{m}$  long, like the one depicted in Fig. 1a. Owing to their strong intrinsic tensile pre-stress, these nanostring resonators exhibit ultra-high quality factors of several 100,000 at room temperature.<sup>12,32</sup> Dielectric transduction combined with a microwave cavity-enhanced heterodyne detection scheme is implemented via two adjacent gold electrodes also apparent in Fig. 1a. The microwave cavity is pumped on resonance at  $\approx 3.6$  GHz to enable displacement detection while avoiding unwanted dynamical backaction effects. The application of a dc voltage as well as a near-resonant rf drive tone  $V_{\text{in}}$  enables actuation and eigenfrequency tuning of the string.<sup>10-12</sup> Moreover, the applied dc voltage also affects the damping rate and the nonlinearity, and introduces strong coupling between the out-of-plane and the in-plane mode when tuned into resonance. For all measurements discussed in the following, a constant dc voltage of 5 V is applied. Under that condition, the fundamental flexural out-of-plane mode can be considered independently, such that the following analysis is performed in the single mechanical mode regime. The experiment is performed under vacuum at a pressure of  $\leq 10^{-4}$  mbar and at room temperature of 293 K.

The sample is characterized by measuring response curves at various drive powers to cali-

brate the measurement (see also Supplementary Information (S.I.).<sup>35</sup>) A weak drive power allows for the characterization of the system in the linear regime. The frequency response of the resonator is measured as a function of the frequency  $f_F$  of the applied rf drive. The measured rf voltage signal is proportional to the resonator's amplitude. The resonance of the fundamental out-of-plane mechanical mode is found at  $f_0 = 6.529$  MHz with a linewidth of  $2\Gamma/2\pi = 20$  Hz, yielding a quality factor of  $Q \approx 325,000$ . Note that this high quality factor is crucial for the presented work as it enables driving the resonator to amplitudes large enough to enter the nonlinear regime and to resolve the satellite peaks appearing in the power spectrum, as discussed in the following.

Increasing the drive power leads to the well-known Duffing response.<sup>36–38</sup> In this model the vibration of the single mode is described by the displacement  $q(t)$  which obeys the equation

$$\ddot{q} + 2\Gamma\dot{q} + \omega_0^2q + \gamma q^3 = F \cos(\omega_F t) + \xi(t). \quad (1)$$

Here,  $\omega_0 = 2\pi f_0$  is the angular eigenfrequency,  $\Gamma$  the damping rate,  $\gamma$  the nonlinearity parameter,  $F$  and  $\omega_F = 2\pi f_F$  are the amplitude and frequency of the external driving, and  $\xi(t)$  is the thermal noise. The effective mass of the resonator is, for the time being, set to  $m = 1$ . In a stationary vibrational state the coordinate  $q(t) = A \cos(\omega_F t + \theta)$  oscillates at the drive frequency with a phase  $\theta$  with respect to the drive. The vibration amplitude  $A$  is given by the solution of the cubic equation  $A_j^2 \{ [\delta\omega - 3\gamma A_j^2 / (8\omega_0)]^2 + \Gamma^2 \} = F^2 / 4\omega_0^2$ , where  $\delta\omega = \omega_F - \omega_0$  is the frequency detuning,  $|\delta\omega| \ll \omega_0$  for the considered resonant driving. This equation reflects the fact that the vibration frequency of a nonlinear resonator depends on its amplitude. It can have one or three positive solutions. In the latter case, only the solutions with the largest and the smallest amplitude,  $A_{hi}$  and  $A_{lo}$ , are stable. An example of the measured amplitude as a function of the

frequency detuning  $\delta\omega$  is shown in Fig. 1b by black dots. The solid line represents a fit of the Duffing model (Eq. (10)). Only one fitting parameter, the nonlinear Duffing parameter  $\tilde{\gamma}$  rescaled to units of  $1/\text{V}^2\text{s}^2$  is required since the eigenfrequency  $\omega_0$ , the damping rate  $\Gamma$  as well as the calibration of the driving force  $F$  are known from the characterization in the linear regime.<sup>35</sup> Nonlinear response curves obtained for different values of the rf drive power  $P = -31$  dBm (shown in Fig. 1b),  $-30$  dBm (shown in the S.I.),  $-25$  dBm,  $-20$  dBm and  $-18$  dBm are fit using a single value  $\tilde{\gamma} = 2.35(15) \cdot 10^{15} \text{V}^{-2}\text{s}^{-2}$ . Further, the backbone of the Duffing curves allows converting the measured amplitude signal (in volts) into real displacement (nanometers).<sup>39</sup> This method relies on the nonlinear Duffing parameter arising from the geometric nonlinearity of the string,  $\gamma^* = 1.54 \cdot 10^{26} \text{m}^{-2}\text{s}^{-2}$ , which corresponds to  $2.28 \cdot 10^{15} \text{V}^{-2}\text{s}^{-2}$  in good agreement with  $\tilde{\gamma}$  extracted from the data.<sup>35</sup>

The theoretical analysis of the resonator dynamics is done by switching to the rotating frame,  $q(t) = x_1(t) \cos(\omega_F t) + x_2(t) \sin(\omega_F t)$  and  $\dot{q}(t) = -\omega_F [x_1(t) \sin(\omega_F t) - x_2(t) \cos(\omega_F t)]$  where the quadratures  $x_1(t)$  and  $x_2(t)$  are new conjugate variables. Using the standard rotating wave approximation (RWA), one finds that the time evolution of these variables is described by the equations

$$\dot{x}_1 = \frac{\partial h(x_1, x_2)}{\partial x_2} - \Gamma x_1, \quad \dot{x}_2 = -\frac{\partial h(x_1, x_2)}{\partial x_1} - \Gamma x_2, \quad (2)$$

with the Hamiltonian function

$$h(x_1, x_2) = \frac{3\gamma}{32\omega_F} (x_1^2 + x_2^2)^2 - \frac{\delta\omega}{2} (x_1^2 + x_2^2) - \frac{F}{2\omega_F} x_1. \quad (3)$$

In writing Eqs. (2) we have, for the time being, disregarded the noise. A contour plot of the function

$h(x_1, x_2)$  in the range of the bistability is shown in Fig. 1c.

A remarkable feature of our high Q nanostring resonator is that the damping rate  $\Gamma$  is small not only compared to the eigenfrequency  $\omega_0$ , but also compared to the frequency detuning  $\delta\omega$  and/or the typical frequency change due to the nonlinearity  $\gamma A_j^2/\omega_F$ . Therefore the damping can be treated as a small perturbation of the Hamiltonian dynamics of an auxiliary “particle” with coordinate  $x_1$  and momentum  $x_2$ . In this limit of weak damping, the extrema  $j = \text{hi, lo}$  of  $h$  correspond to the two stable states of forced vibrations. At the extrema,  $x_{2,j} = 0$ , whereas  $x_{1,j} = A_j$  gives the vibration amplitude, if one disregards corrections  $\propto \Gamma^2$ . The Hamiltonian dynamics for  $\Gamma = 0$  is characterized by the frequency  $\omega_j$  of small-amplitude vibrations about the extrema of  $h(x_1, x_2)$ ,

$$\omega_j = \sqrt{\left[ \frac{9\gamma A_j^2}{8\omega_F} - \delta\omega \right] \left[ \frac{3\gamma A_j^2}{8\omega_F} - \delta\omega \right]}. \quad (4)$$

The frequency is different in the high- and low-amplitude states. In the considered weak-damping case  $\omega_j \gg \Gamma$ .

We now reintroduce noise into the equations for the quadratures and discuss thermal fluctuations around the stable states. Even though the nanoresonator under investigation is small, thermal fluctuations at room temperature are weak. If there is no driving ( $F = 0$  in Eq. (3)), the mean-square values of the quadratures are the same, and for the considered weak nonlinearity  $\langle x_1^2 \rangle = \langle x_2^2 \rangle = k_B T / \omega_0^2$ . Still, even with our highly sensitive detection scheme, we could not resolve the thermal peak in the power spectrum of the resonator in the absence of driving. Resonant driving can make the resonator more sensitive to the noise, i.e., “amplify” fluctuations, as we

discuss, but they still remain small on average.

To analyze the squeezing of fluctuations about the states of forced vibrations for weak damping, we linearize the equations of motion about the stable vibrational states  $(x_{1j}, x_{2j})$  keeping the lowest-order terms in the decay rate  $\Gamma$  (such linearization may be insufficient in the case of extremely weak damping, as discussed in the S.I.). From Eqs. (10) and (2), the resulting equations for the increments  $\delta x_{1,2}$  in the presence of noise are,

$$\begin{pmatrix} \delta \dot{x}_1 \\ \delta \dot{x}_2 \end{pmatrix} = \begin{pmatrix} 0 & -\delta\omega + \frac{3\gamma A_j^2}{8\omega_F} \\ \delta\omega - \frac{9\gamma A_j^2}{8\omega_F} & 0 \end{pmatrix} \begin{pmatrix} \delta x_1 \\ \delta x_2 \end{pmatrix} - \Gamma \begin{pmatrix} (1 + \mu_j)\delta x_1 \\ (1 - \mu_j)\delta x_2 \end{pmatrix} + \begin{pmatrix} \xi_{x_1}(t) \\ \xi_{x_2}(t) \end{pmatrix}. \quad (5)$$

Here,  $\mu_j = 6\gamma A_j^2 / (3\gamma A_j^2 - 8\omega_F \delta\omega)$  and we have disregarded terms  $\propto \Gamma^2$ . Functions  $\xi_{x_1}(t)$  and  $\xi_{x_2}(t)$  describe the noise that drives the quadratures. In the phenomenological model Eq. (10) these functions are given by the real and imaginary parts of  $i\xi(t) \exp(i\omega_F t) / \omega_F$ . If the noise comes from the same coupling to a thermal bath that leads to the vibration decay, on the time scale  $\gg \omega_F^{-1}$  it is zero-mean, Gaussian and  $\delta$ -correlated, and the components  $\xi_{x_1}, \xi_{x_2}$  are independent and have equal intensity,  $\langle \xi_{x_1}(t) \xi_{x_1}(0) \rangle = \langle \xi_{x_2}(t) \xi_{x_2}(0) \rangle = (2\Gamma k_B T / \omega_F^2) \delta(t - t')$ .

A qualitative feature of the driven resonator is that the mean-square fluctuations of the in-phase and quadrature components of the coordinate are no longer equal and can be smaller than in the absence of the drive. This is a squeezing effect. As shown in the S.I.,

$$\langle \delta x_1^2 \rangle = \frac{k_B T}{2m\omega_F^2} (1 + e^{-4\varphi_1}), \quad \langle \delta x_2^2 \rangle = \frac{k_B T}{2m\omega_F^2} (1 + e^{4\varphi_1}). \quad (6)$$

where the expression  $\exp(4\varphi_j) = [\delta\omega - 9\gamma A_j^2 / (8\omega_F)] / [\delta\omega - 3\gamma A_j^2 / (8\omega_F)]$  defines the squeez-

ing parameter  $\varphi_j$ . Here, we have re-introduced the effective mass of the nanoresonator  $m$  to facilitate the comparison with the experiment. In the absence of driving, we find  $A_j = 0$  and thus  $\varphi_j = 0$ , such that we recover the equipartition theorem,  $\langle \delta x_1^2 \rangle = \langle \delta x_2^2 \rangle$ . For the large-amplitude stable state  $\varphi_j \equiv \varphi_{hi} > 0$ , whereas for the small-amplitude state  $\varphi_j \equiv \varphi_{lo} < 0$ . Obviously, the maximum squeezing attainable is a 50 % reduction of the squeezed quadrature according to Eq. (6).

Remarkably the squeezing appears directly in the power spectrum of the resonator.<sup>7,40</sup> In the well-resolved limit  $\Gamma \ll \omega_j$ , one obtains

$$Q_j(\omega) \approx \frac{\Gamma k_B T}{4\pi\omega_F^2} \frac{\cosh 2\varphi_j (1 + \cosh 2\varphi_j)}{(\omega - \omega_F - \Theta_j \omega_j)^2 + \Gamma^2}, \quad |\omega - \omega_F - \omega_j| \ll \omega_j, \quad (7)$$

$$Q_j(\omega) \approx \frac{\Gamma k_B T}{4\pi\omega_F^2} \frac{\cosh 2\varphi_j (\cosh 2\varphi_j - 1)}{(\omega - \omega_F + \Theta_j \omega_j)^2 + \Gamma^2}, \quad |\omega - \omega_F + \omega_j| \ll \omega_j, \quad (8)$$

with  $\Theta_{hi} = +1$  for the large-amplitude stable state and  $\Theta_{lo} = -1$  for the small-amplitude stable state, respectively.<sup>35</sup> The power spectrum  $Q_j(\omega)$  consists of two Lorentzian peaks centered at the frequencies  $\omega_{j+} = \omega_F + \omega_j$  and  $\omega_{j-} = \omega_F - \omega_j$  with the half width given by the damping rate of resonator in the absence of driving  $\Gamma$ . They can be thought of as the Stokes and anti-Stokes components of the Raman scattering of the driving field by the small-amplitude vibrations of the resonator near the corresponding stable state. Importantly, the very state is formed by the drive. This is why the intensities of its components (i.e. the areas of the spectral peaks at  $\omega_{j\pm}$ ) are different in the classical limit considered here. The ratio of the intensities of the two spectral peaks

$$\mathcal{I}_{hi}^{(+)} / \mathcal{I}_{hi}^{(-)} = 1 / \tanh^2(\varphi_{hi}), \quad \mathcal{I}_{lo}^{(+)} / \mathcal{I}_{lo}^{(-)} = \tanh^2(\varphi_{lo}), \quad (9)$$

is determined by the squeezing parameter  $\varphi_j$ . The squeezing parameter can thus be directly extracted from the power spectrum. An advantageous feature of the ratio Eq. (9) is its independence

of the temperature. Therefore even if the nanoresonator is slightly heated by the drive, the ratio of the peak intensities should not change.

To validate these theoretical findings, we apply a resonant sinusoidal drive tone to the fundamental flexural mode of the nanostring ( $f_F = f_0$ ) and record power spectra for different drive powers using a spectrum analyzer operated in the FFT-mode. Under resonant driving, the resonator has one stable vibrational state, with the parameters in Eqs. (6)-(9) corresponding to the high-amplitude state  $A_{\text{hi}}$ . Figure 2a displays power spectra for drive powers in the range between  $-45$  dBm and  $-5$  dBm, with a color coded signal power (dBm). The bright, narrow line centered at zero corresponds to forced vibrations at  $f_F$ . The drive tone is flanked by two satellite peaks. Their separation from the drive tone is symmetric and increases with drive power. We identify these satellites with the thermal noise-induced small-amplitude vibration around the stable state of the driven resonator. Thus the satellite frequencies should be  $\omega_F \pm \omega_{\text{hi}}$ . The experimentally observed satellite separations are compared with the theoretical prediction of Eq. (4), and the resulting satellite positions are shown as open red circles in Fig. 2a. For reasons of visualization, only a few distinct points are plotted. We find the experimental data to coincide with the theory, and also recover the expected scaling of the satellite splitting with drive power  $\omega_{\text{hi}} \propto A_{\text{hi}}^2 \propto F^{2/3} \propto P^{1/3}$ .

Another remarkable feature of the satellites is apparent from their intensities. Figure 2b depicts a line cut extracted from Fig. 2a at  $-20$  dBm. Each satellite is fitted by a Lorentzian with a linewidth of  $2\Gamma/2\pi = 20$  Hz, as shown in Fig. 2b. As predicted by the theoretical model, this linewidth coincides with that of the linear resonance of the string.<sup>35</sup> Clearly, the higher frequency

satellite is much brighter than the lower frequency one. This observation is in agreement with the theoretical model, which predicts non-equal satellite intensities as a result of classical squeezing of the thermal fluctuations. More precisely, as outlined in Eq. (9), for the high-amplitude state  $A_{hi}$ , a higher intensity is expected for the high frequency satellite. Following the model, the ratio of the enclosed satellite areas is related to the squeezing parameter  $\varphi_j$ . The peak areas extracted from the fit are plotted in Fig. 2c as a function of the drive power, where green corresponds to the brighter, higher frequency satellite and blue to the lower frequency satellite. The experimental data are compared with the theoretical predictions which are also included in Fig. 2c as red lines.<sup>35</sup> As suggested by the theoretical model, a pronounced difference in the areas is observed. The ratio of the areas is plotted in Fig. 2d, and again, we find very good agreement between the experimental data (black dots) and the theoretical predictions (red line). We remark that the theoretical calculations of the areas and their ratio shown in Fig. 2 are obtained from a more general analysis of the power spectrum. In a nutshell, this analysis takes into account the non-Lorentzian correction to the shape of the satellites, which becomes particularly important at low drive power and which is not accounted for in the weak damping limit. The area ratio for the weakly damped regime resulting from Eqs. (7) and (8) is also included in Fig. 2d as a gray line. Note that the area ratio in the weakly damped approximation, Eq. (9), is independent of drive power, and denotes the fundamental limit for the area ratio. As a result of the high Q of the nanostring resonator, the measured area ratio approximates this limit for the case of large drive power. A detailed discussion of the two approximations can be found in the S.I.<sup>35</sup>

According to the theory, the satellite peaks in the power spectrum also depend on the detuning

of the drive frequency  $f_F - f_0$ . We therefore repeat the measurement routine, now for a fixed drive power of  $-20$  dBm and a variable detuning of the drive. The resonator is initialized in the high-amplitude state by sweeping up the drive frequency from 30 kHz below  $f_0$  to the desired  $f_F$  before recording the power spectrum. Figure 3a displays the power spectra as a function of the detuning  $f_F - f_0$ . For large negative detuning,  $f_F - f_0 < 0$  only the high frequency satellite can be discerned, the splitting of which from the drive tone increases with increasing  $-(f_F - f_0)$ . For small detuning, both satellites are resolved. They are symmetrically spaced from the drive tone  $f_F$ , with a splitting which only slightly increases with  $f_F - f_0$  for  $f_F - f_0 > 0$ , while their intensity is found to increase. The splitting at zero detuning equals the one shown in the resonantly driven case discussed in Fig. 2a for a drive power of  $-20$  dBm.

Interestingly, the higher frequency satellite vanishes abruptly for a detuning of 190 Hz, whereas the lower frequency one remains. However, the lower satellite exhibits a discontinuity at 190 Hz, and continues with a larger splitting, a different slope, and a strongly reduced intensity. At the same detuning of 190 Hz the amplitude of the drive tone drops to a drastically smaller value, as shown in Fig. 3b. This is a signature of the resonator switching from the high-amplitude state  $A_{\text{hi}}$  to the low-amplitude state  $A_{\text{lo}}$ . The displayed signal power has been extracted from a linecut in Fig. 3a at the driving frequency,  $f = f_F$ . Since every power spectrum in Fig. 3a takes more than one minute to be recorded, this represents a much slower measurement than a typical (Duffing) response curve measurement.

The observed satellites on the opposite sides of the critical detuning  $\Delta f_{\text{cr}} \equiv (f_F - f_0)_{\text{cr}} \approx$

190 Hz are associated with the high- and low-amplitude state  $A_{hi}$  and  $A_{lo}$  of the resonator. They are compared in Fig. 3a with the theoretical prediction for the two stable solutions, which are superimposed to the measured data as red or yellow open circles, respectively. For both cases, we find the experiment and the theory to coincide completely. We repeat the analysis described for the resonantly driven case of Fig. 2, and extract the areas of the high and low frequency satellite of every power spectrum by fitting two Lorentzians (not shown). When the resonator is in the high-amplitude state, i.e. for a detuning below  $\Delta f_{cr}$ , both satellites are resolved and appear for a certain range of detunings. The ratio of the obtained satellite areas within this detuning range is shown in Figure 3c as black dots. Like for the resonantly driven case, this quantity is associated with the squeezing parameter. According to the theoretical model Eq. (9), the area ratio depends on the detuning of the drive frequency. For the case of the high-amplitude solution the area ratio is asymmetric around  $f_0$ , and decreases from negative to positive detuning. The experimental data in Fig. 3c is compared with the theoretical predictions of the area ratio in the weak-damping limit, Eq. (9) (gray line), and the more general approximation that takes into account damping-induced corrections<sup>35</sup> (red line). Once more, the agreement between experiment and theory is remarkable.

Above the switching point,  $f_F - f_0 > \Delta f_{cr}$  the resonator is in the low-amplitude state, and only one satellite is resolved. The area ratio and thus the squeezing parameter cannot be evaluated here. Notice, however, that the data clearly shows the anticipated reversal of the satellite intensities between the two stable solutions predicted by Eq. (9): While the high frequency satellite has the higher intensity for the high-amplitude solution, the low frequency satellite is the dominant one for the low-amplitude solution. In addition, while the area ratio for the high-amplitude solution has

decreased to a value of order 1 in the vicinity of the switching point, the low-amplitude solution exhibits a large area ratio, which explains why the low frequency satellite is resolved but the high frequency satellite cannot be detected. One further observation is that for large positive or negative detuning exceeding 400 Hz, Fig. 3a exhibits only one peak at  $f_F$  resulting in a line with a slope of  $-1$ , as expected for the power spectrum of a thermally driven harmonic oscillator. For even larger detuning, we are not able to resolve the thermal motion of the resonator. We attribute this to an insufficient displacement sensitivity of the detection setup in the absence of driving.

Finally, we discuss the switching between the two stable solutions of the Duffing resonator. The critical switching point is defined as the frequency detuning at which the two transition rates, the one from the high-amplitude state towards the low-amplitude state  $W_{\text{hi} \rightarrow \text{lo}}$  and one from the low-amplitude state towards the high-amplitude state  $W_{\text{lo} \rightarrow \text{hi}}$ , are equal  $W_{\text{hi} \rightarrow \text{lo}} = W_{\text{lo} \rightarrow \text{hi}}$ . For weak damping,  $\Gamma \ll \delta\omega$ , the theoretical value of the critical detuning is estimated<sup>1,41</sup> as  $\delta f_{\text{cr}} \approx 904.6 \frac{1}{\sqrt{2/3} S} \cdot V_{\text{in}}^{2/3}$ , and is included in Fig. 1b as a vertical dashed gray line.

Experimentally, critical switching is only accessible for a slow response measurement, so that the system is always in the most probable state. Clearly, the response curve shown in Fig. 1b does not reveal the critical switching point, since the detuning was swept fast enough to allow the system to stay in the (then metastable) high-amplitude state well beyond that point, until close to the bifurcation point.

By contrast, the linecut extracted from the power spectra shown in Fig. 3b results from a much slower measurement as discussed above, allowing the resonator to approximate its stable

state for every applied detuning. Hence the switching point observed in Fig. 3b should, a priori, be very close to the critical switching point, which is also included as a dashed gray line. Indeed the difference between the gray line indicating the experimentally observed switching and the theoretical critical switching point deviate by only 40 Hz. We attribute this small deviation to the statistical nature of the critical switching point: The observed switching slightly behind the critical point indicates a slightly non-adiabatic frequency sweep, similar to the (even less adiabatic) response curve measurement of Fig. 1b.

To fully characterize the switching, a complementary set of measurements with different sweep times could be used to extract the switching transition rates.<sup>42–44</sup> Furthermore, we note that slow room temperature fluctuations cannot be ruled out as an alternative source of the observed 40 Hz discrepancy despite the fact that  $f_0$  was re-determined prior to every measurement, given a typical eigenfrequency drift of almost 1 kHz/K. We note that the driven resonator is an example of a system without detailed balance. Understanding fluctuation-induced transitions between the stable states of such systems is of interest for various areas of physics, chemistry, and biology. The weak-damping regime attained in the present work is particularly important, as the phase space of the system has more than one dimension, significantly complicating the theoretical analysis of the switching rate. To the best of our knowledge, the present results show the first quantitative comparison with analytical results obtained for such systems.

In conclusion, we report the observation of classical thermal squeezing in the power spectrum of a nonlinear mechanical resonator, without artificial noise or homodyne detection. The

power spectrum of the resonator exhibits two perfectly resolved satellite peaks symmetrically positioned with respect to the drive frequency. They come from the thermally induced small-amplitude vibrations about the stable state of forced vibrations and can be thought of as Stokes and anti-Stokes component in a Raman scattering picture with the caveat that the underlying process is multi-photon, as multiple photons of the resonant driving field are involved. The satellites feature unequal intensities determined by the classical squeezing parameter, which, as we show, can thus be directly read out from the satellites' area ratio. Our findings are supported by a theoretical model which yields excellent agreement with the experimental data with no free parameters. The model shows that, for the resonantly driven underdamped Duffing resonator, the squeezed quadrature can be suppressed by a factor of 2, giving rise to a 3 dB limit like for the case of parametrically induced squeezing.<sup>3</sup> Importantly, no fine tuning is required for obtaining squeezing in a high- $Q$  resonator.

Squeezing of classical fluctuations about the state of forced vibrations in weakly damped nonlinear systems is generic, as it is related to the breaking of the continuous time translation symmetry by the drive. Such systems are broadly used in different areas, and squeezing is of major interest for numerous applications, in particular in high-sensitivity measurements. Our results show that squeezing can be revealed by a standard and comparatively simple analysis of the power spectrum, with no need for homodyne detection. Squeezing of thermal noise in underdamped driven systems is also closely related to the possibility of employing such systems as detectors of weak signals at frequency  $f_S$  close to the drive frequency  $|f_F - f_S| \sim \omega_j$  at room temperature. Squeezing of fluctuations is directly related to resonant amplification of such signals, which can be thought of as multi-photon analog of stimulated Raman scattering, a phenomenon that has not yet

been studied in nanomechanics. Moreover, our results provide an experimental basis for detecting squeezing not only of classical, but also of quantum fluctuations. By extending the analysis<sup>7</sup> we expect such squeezing to occur for a resonantly driven Duffing resonator in spite of the quantum heating effect observed for such a system.<sup>45</sup>

**Acknowledgements** Financial support by the Deutsche Forschungsgemeinschaft via the collaborative research center SFB 767, the European Unions Horizon 2020 Research and Innovation Programme under Grant Agreement No 732894 (FET Proactive HOT), and the German Federal Ministry of Education and Research (contract no. 13N14777) within the European QuantERA cofund project QuaSeRT is gratefully acknowledged. M. I. D. also acknowledges support from the Zukunftskolleg Senior Fellowship at the University of Konstanz and from the National Science Foundation (Grant No. DMR-1806473). Data and analysis code are available at XXX.

**Author Contributions** M.J.S. designed and fabricated the sample. J.S.H. conducted the discussed measurements. M.J.S. and J.K. performed initial measurements. G.R. and M.D. developed the theoretical model. J.S.H., G.R., M.D., and E.M.W. analysed the data and wrote the paper. The results were discussed by all authors.

**Competing Interests** The authors declare that they have no competing financial interests.

**Correspondence** Correspondence and requests for materials should be addressed to E.M.W. (email: eva.weig@uni-konstanz.de).

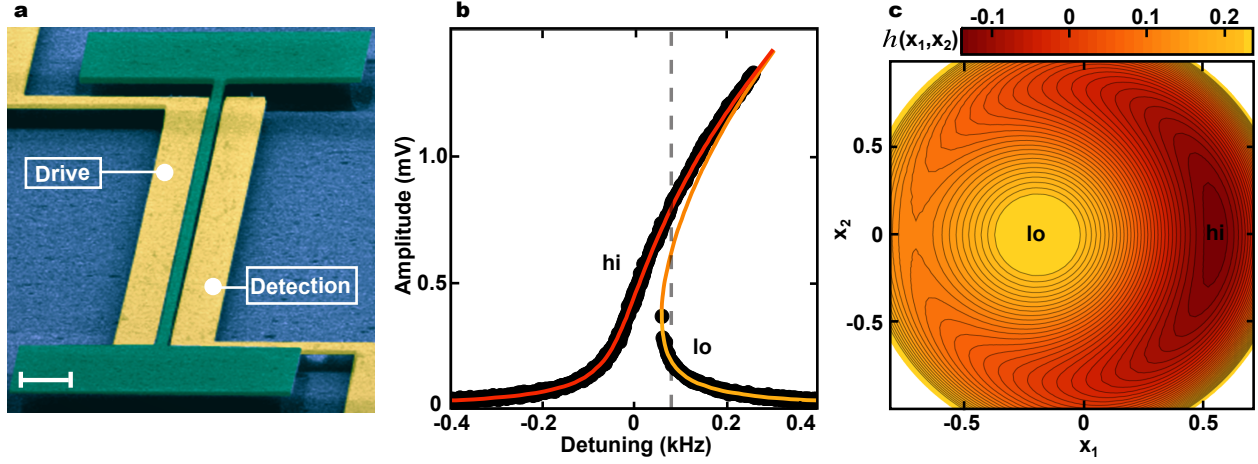


Figure 1: **Nanoelectromechanical system.** **a**, Scanning electron micrograph of the doubly clamped silicon nitride string resonator (green) and two adjacent gold electrodes (yellow) for dielectric control. Schematic of electronic setup is detailed in the S.I. Scalebar corresponds to  $2\ \mu\text{m}$ . **b**, Duffing response curve for an external drive of  $-31\ \text{dBm}$  (black dots) and fit of Eq. (10). The red (yellow) line denotes the high (low) amplitude solution marked “hi” (“lo”), while the orange line represents the unstable solution. Dashed gray line indicates the theoretically calculated critical switching point. **c**, Phase space representation of the effective hamiltonian function  $h(x_1, x_2)$ . Indicated are the high (“hi”, red) and low (“lo”, yellow) amplitude solution. The hamiltonian function  $h(x_1, x_2)$  scaled by  $8\omega_F\delta\omega^2/(3\gamma)$  is plotted using the parameter  $\sqrt{3}\gamma F^2/(32\omega_F^3\delta\omega^3) = 0.013$ , corresponding to the dashed line in (b), whereas the coordinate axes are scaled with  $\sqrt{8\omega_F\delta\omega/(3\gamma)}$ .

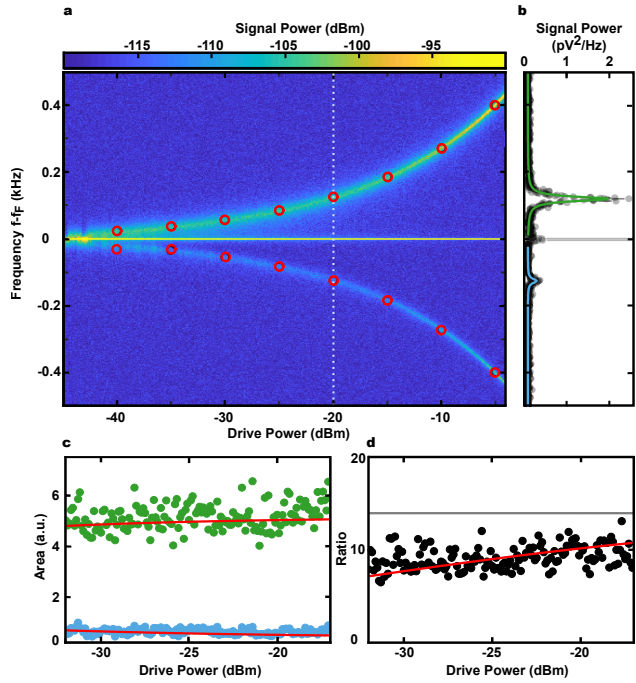


Figure 2: **Power spectra as a function of drive power for a resonant drive frequency.** **a**, Color coded power spectra showing the satellite splitting and intensity (central line at  $f = f_F$  truncated) as a function of the drive power. Red open circles denote the calculated splittings using the theoretical model. **b**, Linecut along the bright dotted line in Fig. 1a illustrating the satellites as well as their Lorentzian fits for a drive of  $-20$  dBm. The central line at  $f = f_F$  (gray line) is truncated. **c**, Area of the high (green) and low (blue) frequency satellite, extracted from the Lorentzian fits, as a function of the drive power. Red lines show the theoretical prediction in the approximation that accounts for the partial overlapping of the tails of the spectral peaks. **d**, Ratio of satellite areas as a function of drive power. Red and gray lines show the theoretical prediction with the account of the small overlapping of the peaks and in the weak-damping limit, respectively.

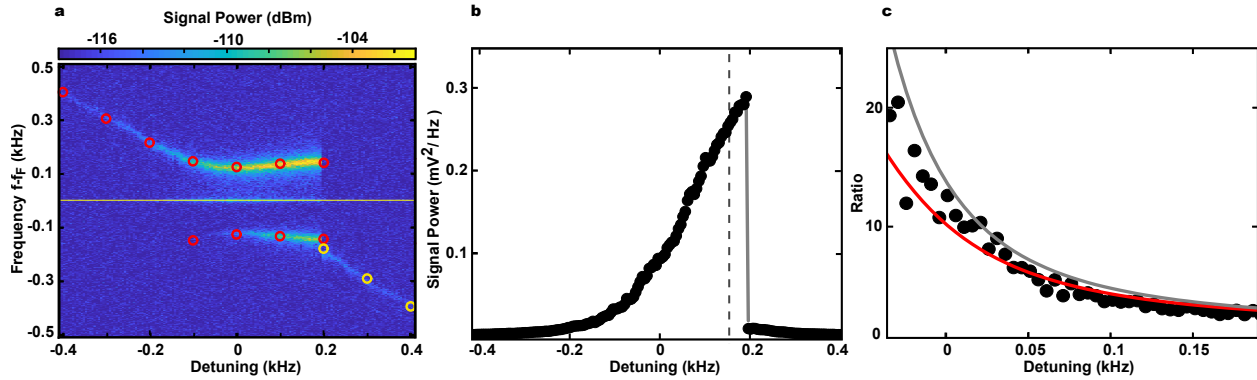


Figure 3: **Power spectra as a function of drive frequency for  $-20$  dBm drive power.** **a**, Color coded power spectra showing the satellite splitting and intensity as a function of the drive frequency detuning. Open circles denote the calculated satellite positions for the high (red) and low (yellow) amplitude solution (see Fig. 1b). **b**, Linecut of Fig. 3a extracting the signal power at the drive frequency  $f_F$  as a function of the detuning. The discontinuity observed at a detuning of 190 Hz indicates the switching of the resonator from the high- to the low-amplitude solution for a slow ramp up of the detuning. It coincides with the discontinuity of the satellites in Fig. 3a. Dashed gray line indicates the theoretically calculated critical switching point. **c**, Ratio of satellite areas for the case of the high-amplitude solution as a function of the detuning. Red and gray lines show the theoretical predictions with and without the account taken of the weak overlapping of the spectral peaks, respectively.

1. Yurke, B. *et al.* Observation of 4.2-K equilibrium-noise squeezing via a Josephson-parametric amplifier. *Physical Review Letters* **60**, 764 (1988).
2. Yurke, B. *et al.* Observation of parametric amplification and deamplification in a Josephson parametric amplifier. *Physical Review A* **39**, 2519 (1989).
3. Rugar, D. & Grütter, P. Mechanical parametric amplification and thermomechanical noise squeezing. *Physical Review Letters* **67**, 699 (1991).
4. Carr, D. W., Evoy, S., Sekaric, L., Craighead, H. G. & Parpia, J. M. Parametric amplification in a torsional microresonator. *Applied Physics Letters* **77**, 1545 (2000).
5. Natarajan, V., DiFilippo, F. & Pritchard, D. E. Classical squeezing of an oscillator for subthermal noise operation. *Physical Review Letters* **74**, 2855 (1995).
6. Stambaugh, C. & Chan, H. B. Supernarrow Spectral Peaks near a Kinetic Phase Transition in a Driven Nonlinear Micromechanical Oscillator. *Physical Review Letters* **97**, 110602 (2006).
7. Almog, R., Zaitsev, S., Shtempluck, O. & Buks, E. Noise Squeezing in a Nanomechanical Duffing Resonator. *Physical Review Letters* **98**, 078103 (2007).
8. Maillet, O. *et al.* Non-linear frequency transduction of nano-mechanical brownian motion. *Physical Review B* **96**, 165434 (2017).
9. Klaers, J. Landauer's erasure principle in a squeezed thermal memory. *Physical Review Letters* **122**, 040602 (2019).

10. DiFilippo, F., Natarajan, V., Boyce, K. R. & Pritchard, D. E. Classical amplitude squeezing for precision measurements. *Physical Review Letters* **68**, 2859 (1992).
11. Szorkovszky, A., Brawley, G. A., Doherty, A. C. & Bowen, W. P. Strong thermomechanical squeezing via weak measurement. *Physical Review Letters* **110**, 184301 (2013).
12. Walls, D. F. Squeezed states of light. *Nature* **306**, 141 (1983).
13. Slusher, R. E., Hollberg, L. W., Yurke, B., Mertz, J. C. & Valley, J. F. Observation of Squeezed States Generated by Four-Wave Mixing in an Optical Cavity. *Physical Review Letters* **55**, 2409 (1985).
14. Wollman, E. E. *et al.* Quantum squeezing of motion in a mechanical resonator. *Science* **349**, 952 (2015).
15. Lecocq, F., Clark, J., Simmonds, R., Aumentado, J. & Teufel, J. Quantum nondemolition measurement of a nonclassical state of a massive object. *Physical Review X* **5**, 041037 (2015).
16. Pirkkalainen, J.-M., Damskagg, E., Brandt, M., Massel, F. & Sillanp, M. Squeezing of quantum noise of motion in a micromechanical resonator. *Physical Review Letters* **115**, 243601 (2015).
17. Caves, C. M. Quantum-mechanical noise in an interferometer. *Physical Review D* **23**, 1693 (1981).
18. Aasi, J. *et al.* Enhanced sensitivity of the LIGO gravitational wave detector by using squeezed states of light. *Nature Photonics* **7**, 613 (2013).

19. Suh, J., LaHaye, M. D., Echternach, P. M., Schwab, K. C. & Roukes, M. L. Parametric amplification and back-action noise squeezing by a qubit-coupled nanoresonator. *Nano Letters* **10**, 3990 (2010).
20. Vinante, A. & Falferi, P. Feedback-enhanced parametric squeezing of mechanical motion. *Physical Review Letters* **111**, 207203 (2013).
21. Poot, M., Fong, K. Y. & Tang, H. X. Classical non-gaussian state preparation through squeezing in an optoelectromechanical resonator. *Physical Review A* **90**, 063809 (2014).
22. Sonar, S. *et al.* Strong thermomechanical squeezing in a far-detuned membrane-in-the-middle system. *Physical Review A* **98**, 013804 (2018).
23. Mahboob, I., Okamoto, H., Onomitsu, K. & Yamaguchi, H. Two-Mode Thermal-Noise Squeezing in an Electromechanical Resonator. *Physical Review Letters* **113**, 167203 (2014).
24. Patil, Y., Chakram, S., Chang, L. & Vengalattore, M. Thermomechanical two-mode squeezing in an ultrahigh-QMembrane resonator. *Physical Review Letters* **115**, 017202 (2015).
25. Pontin, A. *et al.* Dynamical two-mode squeezing of thermal fluctuations in a cavity optomechanical system. *Physical Review Letters* **116**, 103601 (2016).
26. Dykman, M. I. & Krivoglaz, M. A. Theory of fluctuational transitions between stable states of a non linear oscillator. *Soviet Physics JETP* **50**, 30 (1979).
27. Drummond, P. D. & Walls, D. F. Quantum-theory of optical bistability. 1: Non-linear polarizability model. *Journal of Physics A* **13**, 725 (1980).

28. Dykman, M. I. *et al.* Supernarrow spectral peaks and high-frequency stochastic resonance in systems with coexisting periodic attractors. *Physical Review E* **49**, 1198 (1994).
29. Dykman, M. I. Periodically modulated quantum nonlinear oscillators. In Dykman, M. I. (ed.) *Fluctuating Nonlinear Oscillators: from Nanomechanics to Quantum Superconducting Circuits*, 165–197 (Oxford University Press, 2012).
30. Kramers, H. A. Brownian motion in a field of force and the diffusion model of chemical reactions. *Physica (Utrecht)* **7**, 284 (1940).
31. Faust, T., Krenn, P., Manus, S., Kotthaus, J. P. & Weig, E. M. Microwave cavity-enhanced transduction for plug and play nanomechanics at room temperature. *Nature Communications* **3**, 728 (2012).
32. Verbridge, S. S., Parpia, J. M., Reichenbach, R. B., Bellan, L. M. & Craighead, H. G. High quality factor resonance at room temperature with nanostrings under high tensile stress. *Journal of Applied Physics* **99**, 124304 (2006).
33. Unterreithmeier, Q. P., Weig, E. M. & Kotthaus, J. P. Universal transduction scheme for nanomechanical systems based on dielectric forces. *Nature* **458**, 1001 (2009).
34. Rieger, J., Isacsson, A., Seitner, M. J., Kotthaus, J. P. & Weig, E. M. Energy losses of nanomechanical resonators induced by atomic force microscopy-controlled mechanical impedance mismatching. *Nature Communications* **5**, 3345 (2014).
35. See Supplemental Material at (**URL given by editor**) .

36. Landau, L. D. & Lifshitz, E. M. *Theory of Elasticity (Volume 7 of A Course of Theoretical Physics)* (Pergamon, 1970).
37. Nayfeh, A. H. & Mook, D. T. *Nonlinear oscillations* (Wiley, 1995), 7th edn.
38. Dykman, M. *Fluctuating Nonlinear Oscillators: From Nanomechanics to Quantum Superconducting Circuits* (Oxford University Press, 2012), 1 edn.
39. Pernpeintner, M. *et al.* Circuit electromechanics with a non-metallized nanobeam. *Applied Physics Letters* **105**, 123106 (2014).
40. Dykman, M. I., Marthaler, M. & Peano, V. Quantum heating of a parametrically modulated oscillator: Spectral signatures. *Physical Review A* **83**, 052115 (2011).
41. Dmitriev, A. P., D'yakonov, M. I. & Ioff, A. F. Activated and tunneling transitions between the two forced-oscillation regimes of an anharmonic oscillator. *Soviet Physics JETP* **63**, 838 (1986).
42. Aldridge, J. S. & Cleland, A. N. Noise-enabled precision measurements of a duffing nanomechanical resonator. *Physical Review Letters* **94**, 156403 (2005).
43. Stambaugh, C. & Chan, H. B. Noise-activated switching in a driven nonlinear micromechanical oscillator. *Physical Review B* **73**, 172302 (2006).
44. Defoort, M., Puller, V., Bourgeois, O., Pistolesi, F. & Collin, E. Scaling laws for the bifurcation escape rate in a nanomechanical resonator. *Physical Review E* **92**, 050903 (2015).

45. Ong, F. R. *et al.* Quantum heating of a nonlinear resonator probed by a superconducting qubit.  
*Physics Review Letters* **110**, 047001 (2013).

# Supplementary information to "Squeezing of thermal fluctuations in a driven nanomechanical resonator"

## I. THEORY

### I. A. Duffing model

The fundamental mode of the silicon nitride nanostring resonator under investigation is well described by the model of the Duffing resonator. The beam displacement  $q$  at the antinode follows the equation

$$\ddot{q} + 2\Gamma\dot{q} + \omega_0^2 q + \gamma q^3 = F \cos(\omega_F t) + \xi(t), \quad (10)$$

in which  $\Gamma$  is the damping coefficient,  $\omega_0$  is the mode eigenfrequency,  $\gamma$  is the Duffing nonlinearity parameter,  $F$  is the amplitude of the external driving, and  $\omega_F$  is the driving frequency. In our experiment we have  $\gamma > 0$ . The vibrations have inversion symmetry, and therefore there is no term  $\propto q^2$  in Eq. (10). Here for brevity we have set the effective mass of the resonator at the position of the antinode  $m = 1$ ; alternatively, one can think that the forces  $F$  and  $\xi(t)$  incorporate the factor  $1/m$ .

The term  $\xi(t)$  represents the thermal noise. Since the frequency  $\omega_0$  is small compared to  $k_B T/\hbar$  and compared to the reciprocal correlation time of the thermal reservoir (thermal phonons, in our system), the dissipation has no delay and the noise  $\xi(t)$  is zero-mean, Gaussian, and  $\delta$ -correlated. With the effective mass taken explicitly into account, the noise correlator reads  $\langle \xi(t) \rangle = 0$  and  $\langle \xi(t)\xi(t') \rangle = \delta(t - t') 4\Gamma k_B T/m$ , where  $T$  is the room temperature.

It is convenient to switch to the rotating frame and to introduce the scaled complex vibration amplitude  $v$ ,

$$q(t) = \sqrt{\frac{2\omega_F\Gamma}{3\gamma}} [v(t)e^{i\omega_F t} + v^*(t)e^{-i\omega_F t}] , \quad \dot{q}(t) = \sqrt{\frac{2\omega_F\Gamma}{3\gamma}} (i\omega_F) [v(t)e^{i\omega_F t} - v^*(t)e^{-i\omega_F t}] . \quad (11)$$

The relations with the two quadratures defined in the main text are simply  $x_1 = \sqrt{8\omega_F\Gamma/(3\gamma)} \operatorname{Re} v$  and  $x_2 = -\sqrt{8\omega_F\Gamma/(3\gamma)} \operatorname{Im} v$ . In the rotating wave approximation (RWA), we obtain from Eq. (10) the equation of motion for  $v(t)$  in the form

$$\dot{v} = i \frac{\partial h_v}{\partial v^*} - \Gamma v - i\Gamma \xi_v(t); \quad h_v = \Gamma \left[ \frac{1}{2}|v|^4 - \Omega|v|^2 - \beta_v^{1/2}(v + v^*) \right]. \quad (12)$$

Here  $\Omega = \delta\omega/\Gamma$ , with  $\delta\omega = \omega_F - \omega_0$  being the frequency detuning of the drive from the mode eigenfrequency; it is assumed to be small for resonant driving,  $\omega_0, \omega_F \gg |\delta\omega|$ . Parameter  $\beta_v$  is the scaled driving strength and  $\xi_v(t)$  is Gaussian noise,

$$\beta_v = \frac{3\gamma F^2}{32\omega_F^3\Gamma^3}, \quad \xi_v = \sqrt{\frac{3\gamma}{8\omega_F^3\Gamma^3}} \xi(t)e^{-i\omega_F t}, \quad \langle \xi_v(t)\xi_v^*(t') \rangle = \frac{4\alpha}{\Gamma} \delta(t - t'), \quad \alpha = \frac{3\gamma k_B T}{8\omega_F^3\Gamma}. \quad (13)$$

The evolution of  $v(t)$  occurs slowly, on a timescale of  $\sim \Gamma^{-1}$ . On such timescale the correlator  $\langle \xi_v(t)\xi_v(t') \rangle$ , which is fast oscillating in time, can be disregarded, i.e.,  $\xi_v(t)$  is correlated only with  $\xi_v^*(t)$ . The function  $h_v$  is the scaled Hamiltonian  $h$  introduced in Eq. (3) of the main text, see also Fig. 1c.

In the absence of noise, the stationary solutions of Eq. (12) give the scaled complex amplitude

of forced vibrations  $v_j$ , where  $j$  enumerates the solutions,

$$v_j = -\frac{i\beta_v^{1/2}}{1 + i\Omega - i|v_j|^2}, \quad \phi_v(|v_j|^2) = 0,$$

$$\phi_v(x) = x [1 + (x - \Omega)^2] - \beta_v \quad (14)$$

The cubic equation  $\phi_v(|v|^2) = 0$  can have three real roots. This occurs in the region of vibration bistability, which is bounded by the bifurcational values of the dimensional parameter  $\beta_v$

$$(\beta_v)_{B1,2} = \frac{2}{27}[\Omega(\Omega^2 + 9) \pm (\Omega^2 - 3)^{3/2}].$$

The smallest and the largest roots  $|v_j|^2$  correspond to the stable vibrational states of the driven mode (denoted in the main text by lo and hi, respectively), the intermediate root corresponds to an unstable stationary state. The squared resonator amplitudes are  $A_j^2 = (8\omega_F\Gamma/3\gamma)^{1/2}|v_j|^2$  with  $j = \text{hi, low}$ . An example of the dependence of  $A_j$  on the drive frequency is shown as the response function in Fig. 1b of the main text.

## I. B. Linearized dynamics

The noise leads to fluctuations of the driven resonator. For weak noise the major effects are small-amplitude fluctuations about the stable vibrational states and rare events where the noise causes transitions between the states <sup>1</sup>. A simple approach to the analysis of the small-amplitude fluctuations is based on linearizing the equation of motion Eq. (12) about the stable vibrations states <sup>1-3</sup>.

The linearized equations for  $\delta v_j(t) = v(t) - v_j$  read

$$\delta \dot{v}_j(t) = -\Gamma (1 + i\Omega - 2i|v_j|^2) \delta v_j + i\Gamma v_j^2 \delta v_j^* - i\Gamma \xi_v. \quad (15)$$

The dynamics of  $\delta v_j(t)$  is similar to the dynamics of a linear damped harmonic oscillator subject to noise. The characteristic frequency scale of the fluctuations is determined by the eigenvalue of Eq. (15)  $\Gamma\nu_{v,j}$ ,

$$\nu_{v,j}^2 = (3|v_j|^2 - \Omega) (|v_j|^2 - \Omega) + 1 = (\omega_j/\Gamma)^2 + 1 \quad (16)$$

with  $\omega_j$  given by Eq. (4) of the main text. We note that  $\nu_{v,j} \approx \omega_j/\Gamma$  for  $\omega_j \gg \Gamma$ .

### I. C. The power spectrum

Fluctuations of the complex amplitude  $v(t)$  lead to fluctuations of the coordinate  $q(t)$  of the nanoresonator. Such fluctuations are of considerable broad interest, given that the driven nanomechanical resonator is a system far away from thermal equilibrium. They can be directly measured in the experiment by measuring the power spectrum of the nanoresonator. For the periodically driven nanoresonator the power spectrum is defined as

$$Q(\omega) = \frac{1}{\pi} \text{Re} \int_0^\infty dt e^{i\omega t} \bar{Q}(t),$$

$$\bar{Q}(t) = \frac{\omega_F}{2\pi} \int_0^{2\pi/\omega_F} dt' [\langle q(t+t')q(t') \rangle - \langle q(t+t') \rangle \langle q(t') \rangle]. \quad (17)$$

Since the dynamics of the nanoresonator is mostly oscillations at frequency  $\omega_F$  with the amplitude and phase that vary slowly over time  $\sim 1/\omega_F$ , the spectrum  $Q(\omega)$  has peaks centered in a range  $\sim |\delta\omega|, \Gamma$  around the drive frequency  $\omega_F$  (and  $-\omega_F$ , strictly speaking).

Near  $\omega_F$  the spectrum  $Q(\omega)$  is given by the power spectrum of the complex amplitude  $v(t)$ , as seen from Eq. (11),

$$Q(\omega) \approx \frac{2\omega_F\Gamma}{3\pi\gamma} \text{Re} \int_0^\infty dt e^{i(\omega-\omega_F)t} \langle [v^*(t) - \langle v^* \rangle] [v(0) - \langle v \rangle] \rangle. \quad (18)$$

In the range of bistability,  $\langle v \rangle$  is approximately the sum of the values  $v_{\text{hi,lo}}$  weighted with the mean occupation of the corresponding states. For weak noise, these occupations are of the same order of magnitude only in a very narrow parameter range (the region of the kinetic phase transition <sup>1</sup>). Away from this region only one of the stable states is mostly occupied. Also, if the measurement is done over a time which is small compared to the reciprocal rate of interstate transitions,  $\langle v \rangle$  should be replaced by the value  $v_j$  in the state in which the system was prepared. Then  $Q(\omega)$  is given by the partial spectrum

$$Q_j(\omega) = \frac{2\omega_F\Gamma}{3\pi\gamma} \text{Re} \int_0^\infty dt e^{i(\omega-\omega_F)t} \langle \delta v_j^*(t) \delta v_j(0) \rangle. \quad (19)$$

For a long observation time, in addition to the partial spectra given by Eq. (19) the full spectrum  $Q(\omega)$  displays an extremely narrow peak in the region of the kinetic phase transition <sup>3</sup>, which has been seen in micromechanical resonators driven by a noise that imitated a relatively high-temperature thermal noise <sup>4</sup>. In this work we do not consider this peak, since our primary interest focuses on the spectra  $Q_j(\omega)$ .

Calculating  $Q_j(\omega)$  in the region where the motion around the stable states can be linearized and is described by Eq. (15) is straightforward, <sup>2,3</sup>, giving

$$Q_j(\omega) = \frac{\Gamma k_B T}{2\pi\omega_F^2} \frac{(\omega - \omega_F + 2\Gamma|v_j|^2 - \delta\omega)^2 + \Gamma^2(1 + |v_j|^4)}{[(\omega - \omega_F)^2 - \Gamma^2\nu_{v,j}^2]^2 + 4\Gamma^2(\omega - \omega_F)^2}. \quad (20)$$

The total area of the power spectrum Eq. (20) is

$$\mathcal{I}_j \equiv \int d\omega Q_j(\omega) = (k_B T / 2\omega_F^2) \left[ 1 + \frac{|v_j|^4}{\nu_{v,j}^2} \right]. \quad (21)$$

This area exceeds the area of the power spectrum in the absence of the drive, which is given by the above expression with  $|v_j|^2$  set equal to zero. Therefore it turned out to be possible to observe the peaks of the power spectrum of the driven resonator even where in the absence of the driving the resolution of the experiment did not allow us to reliably detect the power spectrum.

For the discussion of the squeezing effect it is convenient to consider the areas of the power spectrum for  $\omega > \omega_F$  and for  $\omega < \omega_F$ , which we denote as  $\mathcal{I}_j^{(+)}$  and  $\mathcal{I}_j^{(-)}$ , respectively. They have the form

$$\mathcal{I}_j^{(\pm)} = \frac{1}{2}\mathcal{I}_j \pm \Delta\mathcal{I}_j, \quad \Delta\mathcal{I}_j = \frac{k_B T}{2\pi\omega_F^2} \frac{2|v_j|^2 - \Omega}{\sqrt{\nu_{v,j}^2 - 1}} \arctan\left(\sqrt{\nu_{v,j}^2 - 1}\right). \quad (22)$$

This expression can be analytically continued in a standard way to the region  $\nu_{v,j} < 1$ . The definition of the peak areas in Eq. (22) takes into account the overlapping of the spectral peaks at  $\pm\Gamma\nu_{v,j}$  for not too large  $\nu_{v,j}$ . This analytic expression is used in the comparison with the experiment in Figs. 2 and 3 of the main text.

The results for the two areas of Eq. (22) are shown in Fig. 4 for the high amplitude state. Here we compare these analytic results with fits of the power spectrum  $Q_j(\omega)$  in the two different frequency ranges,  $\omega > \omega_F$  and  $\omega < \omega_F$ , with a single Lorentzian function, the procedure which was used to extract the satellite areas from the experimental data. Figure 4a and b display the satellite areas as a function of the scaled driving strength  $\beta_v$  and the scaled detuning  $\delta\omega_F/\Gamma$ , respectively. The upper  $x$ -axis converts these values into the real drive power and detuning. The parameters are chosen to match those discussed in Figs. 2b and c, as well as Fig. 3c of the main text. There is a good agreement between the analytic formulas and the fitting.

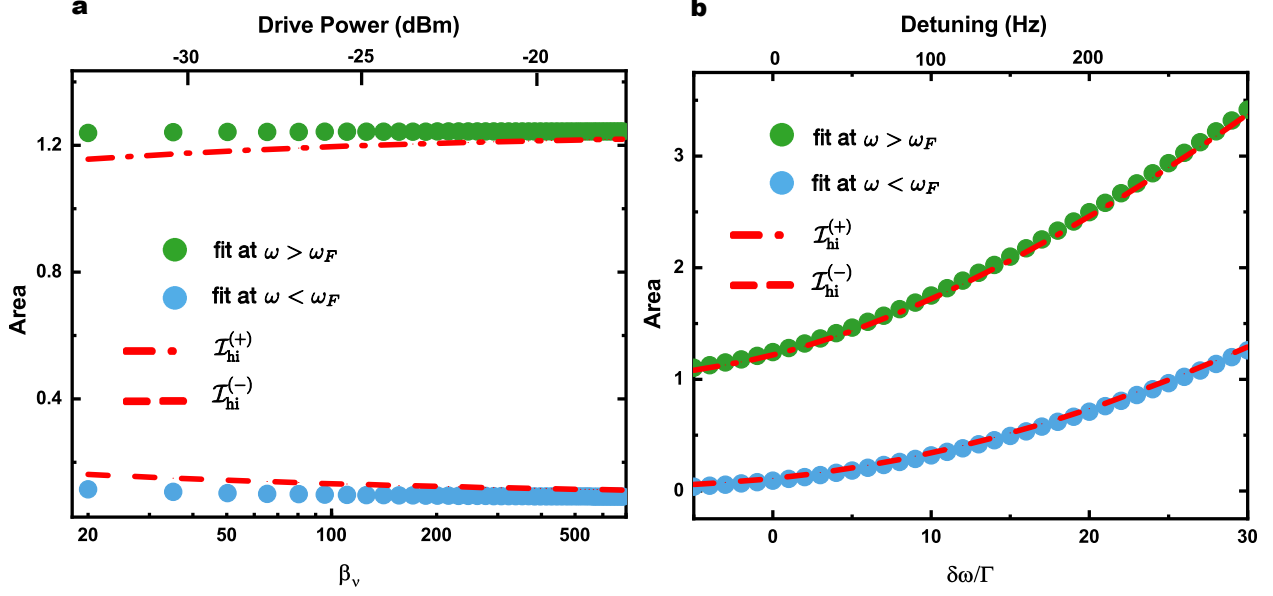


Figure 4: **Areas of the peaks.** The red dash-dotted (dashed) line shows the integral of Eq. (22) for the high (low) amplitude state,  $\mathcal{I}_{hi}^{(+)}$  ( $\mathcal{I}_{hi}^{(-)}$ ), respectively. The integrals are scaled by  $k_B T / (2\omega_F^2)$ . The green and blue dots are obtained by fitting the power spectrum  $Q_{hi}(\omega)$  of Eq. (20) (scaled by  $k_B T / (2\omega_F^2)$ ) in the two frequency ranges,  $\omega > \omega_F$  and  $\omega < \omega_F$ . In both cases, we used a single Lorentzian function for the fitting. **a** Comparison as a function of scaled driving strength  $\beta_v$  at zero detuning  $\delta\omega_F = 0$ . **b** Comparison as a function of scaled detuning  $\delta\omega_F/\Gamma$  at  $\beta_v = 700$ .

#### I. D. Small decay rate: Squeezed thermal fluctuations

The power spectrum  $Q_j(\omega)$  has a particularly simple form in the case of weak damping, where  $\nu_{v,j} \gg 1$ . Here  $Q_j(\omega)$  has two distinct peaks at frequencies  $\omega_{j\pm} = \omega_F \pm \Gamma\nu_{v,j}$ . These peaks are described by Eq. (7) of the main text. Similar peaks emerge in the response of the resonator to an extra drive<sup>1</sup>. The peaks are asymmetric for very small  $\Gamma$ , or equivalently, very large  $\nu_{v,j}$  (still

$\Gamma\nu_{v,j} \ll \omega_0$ ), see below. For not too large  $|\nu_{v,j}|$  they partly overlap. It should be emphasized that the weak-damping condition implied here is much stronger than the condition  $\Gamma \ll \omega_0$  of the nanoresonator to be underdamped. The advantageous feature of the resonator studied in this work is that both conditions are met in the experiment, in a certain range of the amplitude and frequency of the driving field.

To analyze the dynamics in the weak-damping limit we re-write Eqs. (15) separating the terms of the first order in the friction coefficient  $\Gamma$ . From Eq. (14), to the leading order in  $\Gamma$  we have  $v_j^2 \approx \bar{v}_j^2$  with a real positive  $\bar{v}_j^2 \propto \Gamma^{-1}$  given by Eq. (23) below. To the first order in  $\Gamma$

$$v_j \approx \bar{v}_j \left( 1 - \frac{i}{\bar{v}_j^2 - \Omega} \right), \quad \bar{v}_j^2 (\bar{v}_j^2 - \Omega)^2 = \beta_v. \quad (23)$$

Equations (15) for the small deviations  $\delta v_j, \delta v_j^*$  from the stable states can be written as

$$\begin{aligned} \delta \dot{v}_j &= i \frac{\partial \delta h_j}{\partial \delta v_j^*} - \Gamma (\delta v_j + \mu_j \delta v_j^*) - i \Gamma \xi_v(t), \\ \delta h_j &= \Gamma (2\bar{v}_j^2 - \Omega) |\delta v_j|^2 + \frac{1}{2} \bar{v}_j^2 [(\delta v_j^*)^2 + \delta v_j^2]. \end{aligned} \quad (24)$$

Here, the Hamiltonian  $\delta h_j$  is the expansion of the Hamiltonian  $h_v$ , Eq. (12), about  $\bar{v}_j$  to the second order in  $\delta v_j, \delta v_j^*$ . Parameter  $\mu_j = 2\bar{v}_j^2 / (\bar{v}_j^2 - \Omega)$  was introduced in Eq. (5) of the main text. It should be noted that the phase of the scaled complex amplitude  $v_j$  in a stable state  $j$  is “pinned” to the phase of the driving field. This phase directly reflects the broken time-translation symmetry of the stable state. The Hamiltonian  $\delta h_j$  thus also “knows” about the phase of the field. This leads to the terms  $\propto (\delta v_j)^2, (\delta v_j^*)^2$ . If there were no such terms, the quadratures of the fluctuations about the stable state would be equal (we recall that these quadratures are given by the scaled  $\text{Re } \delta v_j$  and  $-\text{Im } \delta v_j$ , respectively). Indeed, as seen from the expression for the correlators  $\xi_v(t)$ , in this case

we would have  $\langle \delta v_j^2 \rangle = \langle (\delta v_j^*)^2 \rangle = 0$ . However, the latter expression does not apply to our driven nonlinear resonator.

Since, as noted above, for weak damping  $v_j \propto \Gamma^{-1/2}$  and  $\Omega \propto \Gamma^{-1}$ , the Hamiltonian  $\delta h_j$  is independent of  $\Gamma$ . This Hamiltonian can be diagonalized by the Bogoliubov (squeezing) transformation

$$\delta v_j = u_j \cosh \varphi_j - u_j^* \sinh \varphi_j, \quad (25)$$

so that the new Hamiltonian for the variables  $u_j$  contains only  $|u_j|^2$  and not  $u_j^2$ ,  $(u_j^*)^2$ . This condition is met if we set

$$\tanh (2\varphi_j) = \frac{\bar{v}_j^2}{2\bar{v}_j^2 - \Omega}. \quad (26)$$

The resulting equation of motion is

$$\begin{aligned} \dot{u}_j &= i \frac{\partial \delta h_j}{\partial u_j^*} - \Gamma u_j - \Gamma \mu_j u_j^* - i \Gamma \xi_j(t), \\ \delta h_j &= \Theta_j \Gamma \nu_{v,j} |u_j|^2, \quad \Theta_j = \text{sgn}(2\bar{v}_j^2 - \Omega), \quad \xi_j(t) = \xi_v(t) \cosh \varphi_j - \xi_v^*(t) \sinh \varphi_j. \end{aligned} \quad (27)$$

In this expression only the leading-order term with respect to  $\Gamma$  should be taken into account in  $\nu_{v,j}$ , i.e.,  $\nu_{v,j} = [(3\bar{v}_j^2 - \Omega)(\bar{v}_j^2 - \Omega)]^{1/2}$ . Clearly,  $\Gamma \nu_{v,j}$  is independent of  $\Gamma$ . The coefficient  $\Theta_j = \pm 1$  is given by the sign of  $2\bar{v}_j^2 - \Omega$ . Parameter  $\varphi_j$  is simply related to the standard <sup>5</sup> parameters  $(r, \theta)$  of the squeezing transformation:  $r = \varphi_j, \theta = 0$  for  $\Theta_j = 1$ , and  $r = |\varphi_j|, \theta = \pi$  for  $\Theta_j = -1$ .

To the lowest order in  $\Gamma$ , the variable  $u_j$  is oscillating as  $\exp[i\Theta_j \Gamma \nu_{v,j} t]$ . The coefficient  $\Theta_j$  reflects the fact that, in the range of bistability,  $u_j$  is rotating in the opposite directions for the large-

and small amplitude stable states where, as it is well-known for the Duffing resonator,  $2\bar{v}_j^2 - \Omega$  is positive or negative, respectively.

Function  $u_j^*(t)$  is rotating in the direction opposite to  $u_j(t)$ . Therefore, for small  $\Gamma$  (or equivalently, for  $\nu_{v,j} \gg 1$ ), the term  $\propto \mu_j$  in Eq. (27) can be disregarded. Then, using the Stratonovich convention for averaging  $\delta$ -correlated noise, we see from Eqs. (13) and (27) that

$$\langle |u_j|^2 \rangle \approx 2\alpha \cosh 2\varphi_j,$$

whereas the mean value  $\langle u_j^2 \rangle \approx -i(2\alpha/\nu_{v,j}) \sinh 2\varphi_j$  is much smaller and can be disregarded. As a result we have for the average values of the quadratures

$$\langle (\text{Re } \delta v_j)^2 \rangle \approx \frac{\alpha}{2} (1 + e^{-4\varphi_j}), \quad \langle (\text{Im } \delta v_j)^2 \rangle \approx \frac{\alpha}{2} (1 + e^{4\varphi_j}), \quad (28)$$

which demonstrates the squeezing of thermal fluctuations about the stable state of forced vibrations. Going back to the unscaled quadratures  $x_1, x_2$ , Eq. (28) gives

$$\langle \delta x_1^2 \rangle = \frac{k_B T}{2\omega_F^2} (1 + e^{-4\varphi_j}), \quad \langle \delta x_2^2 \rangle = \frac{k_B T}{2\omega_F^2} (1 + e^{4\varphi_j}), \quad (29)$$

Equation (27) for  $u_j$  has a simple solution

$$u_j(t) = \exp[-(\Gamma - i\Theta_j \Gamma \nu_{v,j})t] \left[ u_j(0) - i\Gamma \int_0^t dt' \exp[(\Gamma - i\Theta_j \Gamma \nu_{v,j})t'] \xi_j(t') \right]. \quad (30)$$

With this solution, using Eqs. (18) and (25) we obtain

$$\begin{aligned} Q_j(\omega) &\approx \frac{\Gamma k_B T}{4\pi\omega_F^2} \frac{\cosh 2\varphi_j (1 + \cosh 2\varphi_j)}{(\omega - \omega_F - \Theta_j \Gamma \nu_{v,j})^2 + \Gamma^2}, & |\omega - \omega_F - \Theta_j \Gamma \nu_{v,j}| \ll \Gamma \nu_{v,j}, \\ Q_j(\omega) &\approx \frac{\Gamma k_B T}{4\pi\omega_F^2} \frac{\cosh 2\varphi_j (\cosh 2\varphi_j - 1)}{(\omega - \omega_F + \Theta_j \Gamma \nu_{v,j})^2 + \Gamma^2}, & |\omega - \omega_F + \Theta_j \Gamma \nu_{v,j}| \ll \Gamma \nu_{v,j}. \end{aligned} \quad (31)$$

The power spectrum Eq. (31) coincides with Eq. (7) of the main text if one takes into account that  $\Theta_j = 1$  for the high amplitude stable state and  $\Theta_j = -1$  for the low amplitude stable state. The spectrum consists of two Lorentzian peaks with half width  $\Gamma$ . The peaks are located at the drive frequency shifted up and down by the frequency of vibrations in the rotating frame about the stable state  $j$ . We emphasize that, since we kept only the leading-order terms in the decay rate  $\Gamma$ , Eq. (31) applies only in the frequency ranges of the peaks.

It is instructive also to compare the areas of the peaks described by Eq. (31) with Eq. (22) for the areas of the peaks on the opposite sides of  $\omega_F$ . From Eq. (31), the areas of the peaks are

$$\mathcal{I}_j^{(\pm)} = \frac{k_B T}{4\omega_F^2} \cosh 2\varphi_j (\cosh 2\varphi_j \pm 1) = \frac{k_B T}{4\omega_F^2} \left[ 1 + \frac{\bar{v}_j^4}{\nu_{v,j}} \pm \frac{2\bar{v}_j^2 - \Omega}{\nu_{v,j}} \Theta_j \right] \quad (32)$$

One can easily see that this expression coincides with Eq. (22) if in the latter equation one goes to the limit  $\nu_{v,j} \gg 1$  and replaces  $|v_j|^2$  with  $\bar{v}_j^2$ , which corresponds to keeping the terms of the lowest-order in  $\Gamma$ .

The central feature of the spectrum Eq. (31) is that the two spectral peaks of  $Q_j(\omega)$  have different amplitudes and areas. This is a direct indication of the squeezing of the vibrations about the stable state. Measuring the ratio of the peak heights allows one to directly determine the squeezing parameter  $\varphi_j$  and thus, if we use the conventional notations of quantum optics, the squeezing parameter  $r = |\phi_j|$ .

### I. E. Asymmetry of the spectral peaks for small decay rate

In calculating the spectral peaks  $Q_j(\omega)$  in the previous section we expanded the Hamiltonian  $h_v$  to

second order in  $\delta v, \delta v^*$ . Disregarding higher-order terms is inconsistent, generally, in the limit of small decay rate  $\Gamma$ . These terms describe the nonlinearity of the vibrations about the stable states in the rotating frame. Such nonlinearity leads to the dependence of the vibration frequency on the vibration amplitude. Thermal fluctuations of the amplitude then translate into thermal fluctuations of the vibration frequency and thus lead to broadening of the spectral peaks of  $Q_j(\omega)$ . Such broadening is well understood for nonlinear resonators in the absence of strong periodic driving <sup>6</sup>.

A quantum theory of the nonlinearity-induced spectral broadening of the peaks of  $Q_j(\omega)$  was discussed in Ref. [7]. Here we will briefly outline the corresponding classical theory. As indicated in the main text, the amplitude dependence of the vibration frequency comes from the Duffing nonlinearity in the first order of the perturbation theory. More generally, it is well-known from classical mechanics <sup>8</sup> that the first-order terms in the amplitude dependence of the vibration frequency come from the terms in the Hamiltonian that are nonzero when averaged over the vibration period. In the case of the Duffing resonator the corresponding term is  $\gamma q^4/4$  which, for  $q = A \cos(\omega_0 t + \phi)$ , has the period-averaged value  $3\gamma A^4/32$ .

In line with the above argument, to find the amplitude dependence of the vibrations in the rotating frame about a  $j$ th state one has to do the following steps:

- Expand the full Hamiltonian  $h_v$  about  $\bar{v}_j$  to the 4th order in  $\delta v_j, \delta v_j^*$ .
- Express  $\delta v, \delta v^*$  in terms of  $u_j, u_j^*$
- Out of all quartic terms in  $u_j, u_j^*$  keep only the term  $\propto |u_j|^4$ , as this is the only term that does not oscillate in the harmonic approximation.

The above routine has to be augmented to allow for the fact that the cubic terms  $\delta h_j^{(3)} = \bar{v}_j |\delta v_j|^2 \cdot (\delta v_j + \delta v_j^*)$  will contribute to the amplitude dependence of the frequency when taken to the second order of the perturbation theory. The corresponding terms renormalize the coefficient in front of the term  $\propto |u_j|^4$ . The result is as if the relevant quartic term in  $u_j, u_j^*$  of the effective Hamiltonian has the form

$$\begin{aligned} \delta h_j^{(4)} &= \frac{1}{2} \Gamma B_j |u_j|^4, \\ B_j &= \frac{1}{2} (3 \cosh^2 2\varphi_j - 1) - \frac{\bar{v}_j^2 \exp(-2\varphi_j)}{\Theta_j \nu_{v,j}} \left( \frac{9}{2} \cosh 4\varphi_j - 3 \sinh 4\varphi_j + \frac{3}{2} \right). \end{aligned} \quad (33)$$

The parameter  $B_j$  is determined by the ratio  $\beta = \beta_v / \Omega^3$ . A plot of  $V = 2B_j$  and  $\nu_0 = \nu_{v,j} / \Omega$  as functions of this ratio for the large- and small-amplitude attractor is shown in Fig. 9 of Ref. [7].

The Hamiltonian  $\delta h_j^{(4)}$  has to be added to  $\delta h_j$  in the equation of motion for  $u_j$ , Eq. (27). The resulting equation has the same general form as the equation of motion of an anharmonic Duffing resonator with eigenfrequency  $\Gamma \Theta_j \nu_{v,j}$  in the presence of relaxation and noise, but with no driving. Using the results <sup>7,9</sup> we can write the power spectrum of the resonator near frequency  $\omega_F + \Gamma \Theta_j \nu_{v,j}$  in the form of a series

$$\begin{aligned} Q_j(\omega) &\approx \frac{k_B T}{4\pi\omega_F^2} \cosh 2\varphi_j (\cosh 2\varphi_j + 1) \text{Re} \sum_n \phi_j(n, \omega - \omega_F - \Gamma \Theta_j \nu_{v,j}), \\ \phi_j(n, \omega') &= 4n (\Lambda_j - 1)^{n-1} (\Lambda_j + 1)^{-(n+1)} [\Gamma (2\aleph_j n - 1) - i\omega']^{-1}. \end{aligned} \quad (34)$$

Here,

$$\Lambda_j = (1 + 2iB_j\alpha \cosh 2\varphi_j) / \aleph_j, \quad \aleph_j = (1 + 4iB_j\alpha \cosh 2\varphi_j)^{1/2} \quad [\text{Re } \aleph_j > 0]. \quad (35)$$

Near frequency  $\omega_F - \Gamma\Theta_j\nu_{v,j}$  the power spectrum has the form

$$Q_j(\omega) \approx \frac{k_B T}{4\pi\omega_F^2} \cosh 2\varphi_j (\cosh 2\varphi_j - 1) \operatorname{Re} \sum_n \phi_j[n, -(\omega - \omega_F + \Gamma\Theta_j\nu_{v,j})]. \quad (36)$$

The shape of the spectra in Eqs. (34) and (36) is determined by the parameter  $B_j\alpha$ , i.e., by the effective nonlinearity of the vibrations about the stable vibrational state. If  $|B_j|\alpha \ll 1$ , the main contribution to the spectra comes from the term  $n = 1$  and the spectra are close to the Lorentzian spectra of Eq. (31). However, if  $|B_j|\alpha \gtrsim 1$ , the shape of the spectral peaks strongly differs from the Lorentzian shape. Since  $|B_j| \sim 1$ , the important parameter of the spectral shape is  $\alpha$ . This parameter characterizes the ratio of the broadening of the spectrum due to thermal fluctuations of the vibration amplitude and the decay rate. Equations (34) and (36) allow one to calculate the shape of the spectrum for an arbitrary  $\alpha$  and to see the evolution of the spectrum with increasing  $\alpha$ .

We wish to make the following two comments: First, the nonlinearity of the vibrations about the stable states, although it can dramatically change the shape of the peaks at frequencies  $\omega_F \pm \Theta_j\Gamma\nu_{v,j}$  for weak damping, does not change the area of these peaks, to the leading order. Second, it is important to keep in mind that Eq. (31) applies in the intermediate range of the decay rate. The decay rate has to be small, so that the spectral peaks described by Eq. (31) are well resolved. However, it should be not too small if one approximates the shape of the peaks by a Lorentzian.

## II. EXPERIMENTAL SETUP, CHARACTERIZATION and CALIBRATION

### II. A Sample and experimental measurement setup

The nanomechanical resonator under investigation is a doubly clamped silicon nitride string resonator. It is 270 nm wide, 100 nm thick and 55  $\mu\text{m}$  long and flanked by two adjacent gold electrodes for dielectric control. A schematic of the dielectric measurement setup is depicted in Fig. S1. A microwave signal ( $\mu\text{W}$ ) is used to resonantly pump the microwave cavity, which is bonded to one of the electrodes. The transmitted and modulated microwave cavity signal (RF) is demodulated by IQ-mixing it with a reference signal (LO). The output signal is low-pass filtered (LP), amplified (AMP) and its frequency spectrum is recorded using a spectrum analyzer (SA). Only for the measurement shown in Fig. 1b of the main text as well as Fig. S2, a lock-in amplifier is employed. The dc voltage (dc) and the rf drive tone (rf) of frequency  $f_F$  are combined with a bias tee and applied to the other electrode. A microwave bypass enables the combination of dielectric actuation and detection. More details about the dielectric control scheme can be found in Refs. 10–12.

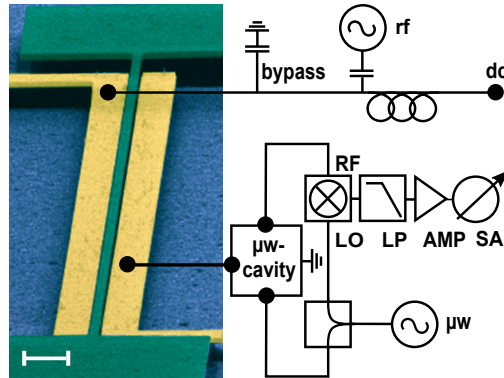


Figure 5: **Setup.** Simplified electronic set-up for dielectric actuation and displacement detection. Scalebar of scanning electron micrograph corresponds to 2  $\mu\text{m}$ .

## II. B Calibration using the linear response function

In the measurement we cannot access the amplitude  $A$  and the force  $F$  directly. However we know the amplitude of the rf input voltage  $V_{\text{in}}$  that drives the capacitor containing the dielectric nanostring and we measure the output voltage signal  $V_{\text{out}}$  close to the eigenfrequency of the resonator  $\omega_0$ . We assume these quantities to be proportional to the driving strength  $F$  and to the amplitude  $A$ , respectively,

$$A = a V_{\text{out}} \quad , \quad F = b V_{\text{in}} \quad . \quad (37)$$

This allows us to calibrate the driving strength with the benefit of excluding a parameter for further analysis. For weak driving power, the resonator is in the linear regime and the vibration amplitude  $A$  is given by the well known Lorentzian response  $A^2 = (F/2\omega_0)^2 / (\delta\omega^2 + \Gamma^2)$ . Rewriting the Lorentzian response function with the use of Eq. (37) leads to

$$V_{\text{out}}^2 = \frac{\Gamma^2}{\delta\omega^2 + \Gamma^2} \cdot c \cdot V_{\text{in}}^2, \quad (38)$$

where the dimensionless parameter  $c = (b/a)^2 / (4\omega_0^2\Gamma^2)$  is the calibration factor. At fixed rf input voltage  $V_{\text{in}}$  (or drive power), we fit  $V_{\text{out}}$  with the Lorentzian function Eq. (38) (see Fig. S2a), yielding an eigenfrequency  $f_0 = \omega_0/2\pi = 6.529$  MHz and a linewidth  $2\Gamma/2\pi = 20$  Hz. The same linewidth is found by a ringdown measurement (see Fig. S2b).

Driving the system on resonance ( $\delta\omega = 0$ ) gives the maximum output signal  $V_{\text{out,max}}$ , and it follows that  $V_{\text{out,max}}^2 = c V_{\text{in}}^2$ . This procedure is repeated for different drive voltages  $V_{\text{in}}$  (expressed as drive power in the main text). The obtained ratios  $V_{\text{out,max}}^2/V_{\text{in}}^2$  are fit with the constant  $c$ . We obtained a calibration factor  $c = 0.0062(3)$ .

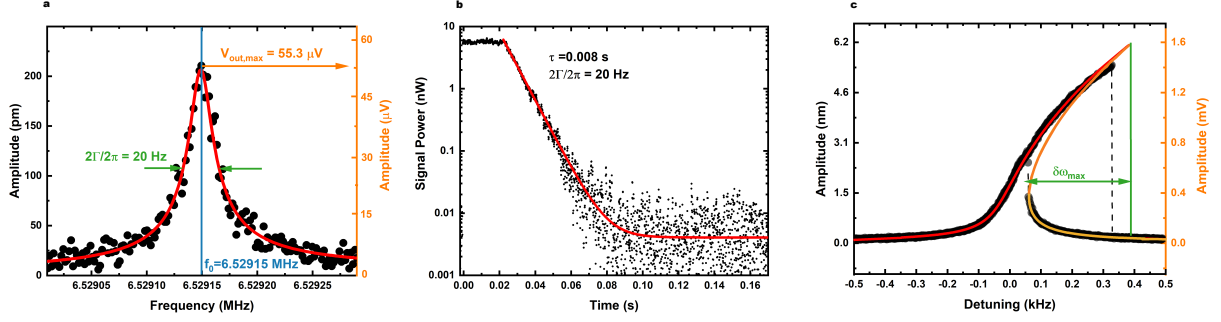


Figure 6: **Characterization and calibration of system properties.** **a**, Linear response measurement (black dots) as well as Lorentzian fit (red line) for the eigenfrequency and linewidth evaluation as well as for the driving strength calibration. **b**, Ringdown measurement (black dots) along with exponential fit (red line), confirming the linewidth measured in linear response. **c**, Nonlinear response measurement (black dots) with fit of the Duffing model (red, yellow, and orange line represents stable high amplitude, stable low amplitude and unstable solution, respectively). Amplitude and frequency detuning of the backbone point highlighted in green are used for the amplitude calibration.

## II. C Duffing nonlinearity parameter

From Eq. (14) one can express the detuning  $\delta\omega$  in terms of the amplitude  $A$  of the forced vibrations on the high-amplitude branch. Using the scaling relations Eq. (37), we can write

$$\frac{\delta\omega}{\Gamma} = \frac{3\tilde{\gamma}}{8\omega_0\Gamma} V_{\text{out}}^2 - \sqrt{c \left( \frac{V_{\text{in}}^2}{V_{\text{out}}^2} \right) - 1}, \quad (39)$$

where we have introduced an effective Duffing parameter  $\tilde{\gamma} = \gamma \cdot a^2$  with dimension  $[1/V^2s^2]$ . In the non-linear regime, we fit the nonlinear amplitude response function by plotting  $\delta\omega$  as a function

of the r.h.s. of Eq. (39) with the high amplitude branch for  $V_{\text{out}}$  and using  $\tilde{\gamma}$  as the single fitting parameter. For the power  $P = -31$  dBm, which is used to obtain the results shown in Fig. 1b of the main text, and for  $P = -30$  dBm used shown in Fig. S2c we found the scaled Duffing parameter to be  $\tilde{\gamma} = 2.35 \cdot 10^{15} \text{ V}^{-2} \text{ s}^{-2}$ . With the measured calibration factor  $c$ , the scaled Duffing parameter  $\bar{\gamma}$ , the eigenfrequency, and the decay rate of the mode, we have fully determined the parameters of the theoretical model, Eq.(1) of the main text, except for the scaling for thermal fluctuations  $a$ .

## II. D Amplitude calibration via the Duffing backbone curve

In order to compare the theoretical and experimental results on the power spectra we need to scale the fluctuation intensity. We note that the fluctuation-dissipation relation on its own is not sufficient unless we know the actual displacement of the nanobeam at the antinode and the effective mass of the nanobeam. From the linear relation  $A = a V_{\text{out}}$ , one has the relation  $Q_{VV}(\omega) = Q(\omega)/a^2$  with  $Q_{VV}(\omega)$  being the power spectrum of the output voltage, and  $Q(\omega)$  being the power spectrum of the resonator displacement in the linear regime. In the absence of driving we expect  $\int d\omega Q_{VV}(\omega) = k_B T / (2 m \omega_0^2 a^2)$ . By measuring the power spectrum and calculating the total area of the Lorentzian, one can extract the coefficient  $a$ . However we can not resolve the thermal motion of the undriven nanostring in our system apparatus and therefore we use another strategy.

To convert the voltage signal (measured in volts) into displacement amplitude (measured in nm) we use the fact that, in the Duffing model, the maximum value of the amplitude of forced vibrations as a function of the frequency detuning is given by the the so-called backbone equation

$$\frac{3\gamma}{8\omega_0} A_{\text{max}}^2 = \delta\omega_{\text{max}} \quad (40)$$

in which  $\delta\omega_{\max}$  denotes the detuning at which the upper bifurcation point is reached. To relate the the measured voltage  $V_{\text{out,max}}$  to the maximal displacement  $A_{\max} = V_{\text{out,max}}/a$  we use the measured  $\delta\omega_{\max}$  and the value of  $\gamma$  that we calculate assuming that the nanoresonator is a string, the nonlinearity of which is solely determined by its geometric nonlinearity  $\gamma^*$ , using the expression

$$\gamma^* = \pi^4 \frac{E + \frac{3}{2}\sigma}{4l^4\rho} = 1.54 \cdot 10^{26} \text{ m}^{-2}\text{s}^{-2}, \quad (41)$$

where  $E$  is the Young's modulus,  $\sigma$  the tensile stress and  $\rho$  the mass density. For our suspended silicon nitride nanostring (atop a fused silica substrate) the tensile stress is measured to be  $\sigma = 1.46 \text{ GPa}$ ,<sup>12</sup> while Young's modulus yields  $E = 169 \text{ GPa}$ .<sup>13</sup> The density  $\rho = 2800 \text{ kg/m}^3$  is reported in literature.<sup>14</sup>

In this way we relate the maximum of the Duffing backbone curve, measured in volts, to the amplitude measured in nm as shown in Fig. S1c. The found proportional factor  $a = 3.9 \cdot 10^{-6} \text{ m/V}$  is also used for the amplitude of the linear response measurement, plotted in Fig. S1a.

It is important to compare the resulting Duffing nonlinearity parameter  $\tilde{\gamma}^* = \gamma^* \cdot a^2$  determined from the calculated  $\gamma^*$  and the calibration factor  $a$  with the measured  $\tilde{\gamma}$ . We used  $\gamma^* = 1.54 \cdot 10^{26} \text{ m}^{-2}\text{s}^{-2}$ , which gave us  $a = 3.9 \cdot 10^{-6} \text{ m/V}$ , and thus  $\tilde{\gamma}^* = \gamma^* \cdot a^2 = 2.28 \cdot 10^{15} \text{ V}^{-2}\text{s}^{-2}$ . The fitted Duffing nonlinearity parameter is  $\tilde{\gamma} = 2.35 \cdot 10^{15} \text{ V}^{-2} \text{ s}^{-2}$ , which is in reasonably good agreement.

## II. E Additional data

As an additional measurement we apply a fixed detuning of 190 Hz to the actuation frequency

(close to the measured critical switching point) and sweep the drive power from -45 dBm up to -4 dBm, comparable to the measurement under resonant drive in the main text (Fig. 2a). The resulting power spectra as a function of drive power are shown in Fig. S3a. In contrast to the data obtained for a resonant drive, we observe an additional, single lower frequency satellite. This satellite is observed for a weak drive (below -30 dBm). For a strong drive (above 15 dBm), two symmetrical satellites are observed, similarly to the data obtained for a resonant drive. In the regime in between, each power spectrum shows either the former or the latter satellites, such that both satellite branches are visible. By calculating the expected satellite splitting, we can assign the single satellite to the low amplitude state of the Duffing resonator (yellow circles) and the two symmetric satellites to the high amplitude state (red circles). In the intermediate drive range, the Duffing resonator is in the bistable regime and depending on the initial conditions the system chooses either the high or the low amplitude solution, consequently we see a switching behaviour between the two possible satellite branches. This is particularly apparent from Fig. S3b, which plots the amplitude response at the drive tone as a function of the drive power, as in Fig. 3b of the main text. For a weak drive (below -25 dBm), the resonator is always in the low amplitude state, whereas for a large drive (above 15 dBm), the system is only found in the high amplitude state. In the intermediate region, the amplitudes jumps back and fourth, leading to the behavior observed for the satellite branches. As before, the area of the satellites can be extracted by a Lorentzian fit and the calculated ratio of the areas is plotted in Fig. S2c. We can only report a ratio for the high amplitude solution, as only one of the two satellites of the low amplitude solution is resolved in the experiment. Again the calculated area ration is in a good agreement with the theory, where the

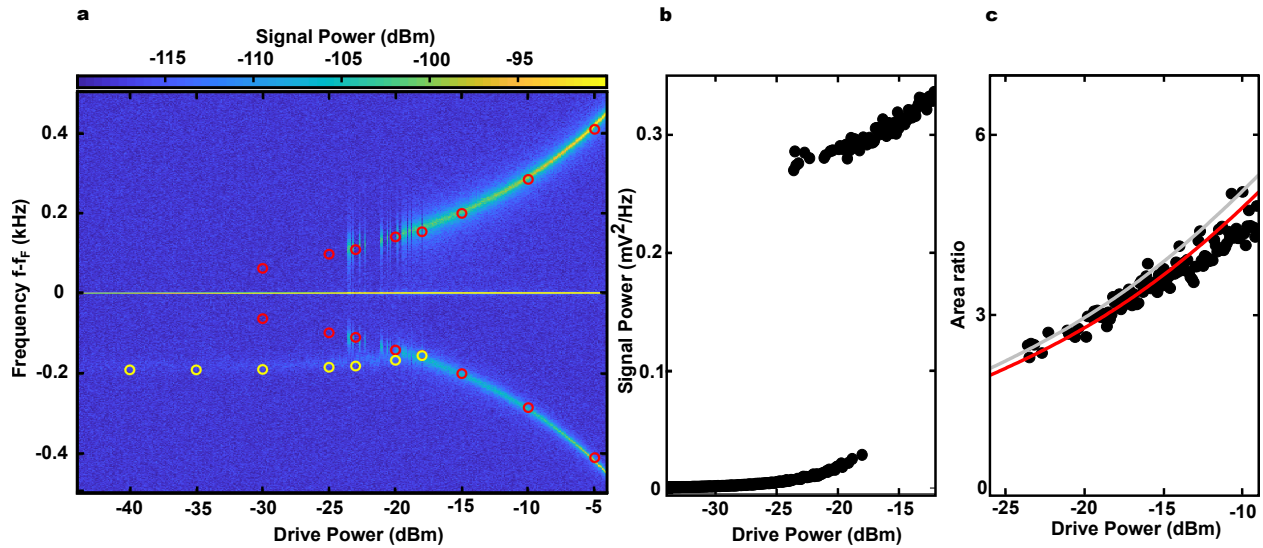


Figure 7: **Power spectra as a function of the drive power for a fixed detuning of 190 Hz.** **a**, Color coded power spectra showing the satellite splitting and intensity as a function of the drive power. Red (yellow) open circles denote theoretically calculated satellite positions for the high (low) amplitude solution. **b**, Extracted amplitude of the response at the drive tone as a function of the drive power. **c**, Ratio of the satellite areas when the resonator is in the high amplitude state. Red (gray) line shows the theoretical prediction in the linear (weak damping) approximation.

red line corresponds to the more general linear approximation and the gray line to the additional weak damping approximation.

1. Dykman, M. I. & Krivoglaz, M. A. Theory of fluctuational transitions between stable states of a non linear oscillator. *Soviet Physics JETP* **50**, 30 (1979).
2. Drummond, P. D. & Walls, D. F. Quantum-theory of optical bistability. 1: Non-linear polariz-

- ability model. *Journal of Physics A* **13**, 725 (1980).
3. Dykman, M. I. *et al.* Supernarrow spectral peaks and high-frequency stochastic resonance in systems with coexisting periodic attractors. *Physical Review E* **49**, 1198 (1994).
  4. Stambaugh, C. & Chan, H. B. Supernarrow Spectral Peaks near a Kinetic Phase Transition in a Driven Nonlinear Micromechanical Oscillator. *Physical Review Letters* **97**, 110602 (2006).
  5. Walls, D. F. & Milburn, G. J. *Quantum Optics* (Springer, Berlin, 2008).
  6. Dykman, M. I. & Krivoglaz, M. A. Theory of nonlinear oscillations interacting with a medium. *Physical Review* **5**, 265–441 (1984).
  7. Dykman, M. I. Periodically modulated quantum nonlinear oscillators. In Dykman, M. I. (ed.) *Fluctuating Nonlinear Oscillators: from Nanomechanics to Quantum Superconducting Circuits*, 165–197 (Oxford University Press, 2012).
  8. Arnold, V. I. *Mathematical Methods of Classical Mechanics* (Springer, New York, 1989).
  9. Dykman, M. I. & Krivoglaz, M. A. Classical theory of nonlinear oscillators interacting with a medium. *Phys. Stat. Sol. B* **48**, 497–& (1971).
  10. Unterreithmeier, Q. P., Weig, E. M. & Kotthaus, J. P. Universal transduction scheme for nanomechanical systems based on dielectric forces. *Nature* **458**, 1001 (2009).
  11. Rieger, J., Isacsson, A., Seitner, M. J., Kotthaus, J. P. & Weig, E. M. Energy losses of nanomechanical resonators induced by atomic force microscopy-controlled mechanical impedance mismatching. *Nature Communications* **5**, 3345 (2014).

12. Faust, T., Krenn, P., Manus, S., Kotthaus, J. P. & Weig, E. M. Microwave cavity-enhanced transduction for plug and play nanomechanics at room temperature. *Nature Communications* **3**, 728 (2012).
13. Unterreithmeier, Q. P., Faust, T. & Kotthaus, J. P. Damping of nanomechanical resonators. *Physical Review Letters* **105** (2010).
14. Gad-el Hak, M. *The MEMS Handbook* (CRC Press, 2002).